

# Micro-probing enables fine-grained mapping of neuronal populations using fMRI

Joana Carvalho<sup>a,\*</sup>, Azzurra Invernizzi<sup>a</sup>, Khazar Ahmadi<sup>c</sup>, Michael B. Hoffmann<sup>c,d</sup>, Remco J. Renken<sup>a,b</sup>, Frans W. Cornelissen<sup>a</sup>

<sup>a</sup> Laboratory of Experimental Ophthalmology, University Medical Center Groningen, University of Groningen, Groningen, Netherlands

<sup>b</sup> Cognitive Neuroscience Center, University Medical Center Groningen, University of Groningen, Netherlands

<sup>c</sup> Department of Ophthalmology, Otto-von-Guericke University, Magdeburg, Germany

<sup>d</sup> Center for Behavioral Brain Sciences, Magdeburg, Germany

## ARTICLE INFO

### Keywords:

Visual field mapping  
Receptive field  
fMRI  
Computational modelling

## ABSTRACT

The characterization of receptive field (RF) properties is fundamental to understanding the neural basis of sensory and cognitive behaviour. The combination of non-invasive imaging, such as fMRI, with biologically inspired neural modelling has enabled the estimation of population RFs directly in humans. However, current approaches require making numerous *a priori* assumptions, so these cannot reveal unpredicted properties, such as fragmented RFs or subpopulations. This is a critical limitation in studies on adaptation, pathology or reorganization. Here, we introduce micro-probing (MP), a technique for fine-grained and largely assumption free characterization of multiple pRFs within a voxel. It overcomes many limitations of current approaches by enabling detection of unexpected RF shapes, properties and subpopulations, by enhancing the spatial detail with which we analyze the data. MP is based on tiny, fixed-size, Gaussian models that efficiently sample the entire visual space and create fine-grained probe maps. Subsequently, we derived population receptive fields (pRFs) from these maps. We demonstrate the scope of our method through simulations and by mapping the visual fields of healthy participants and of a patient group with highly abnormal RFs due to a congenital pathway disorder. Without using specific stimuli or adapted models, MP mapped the bilateral pRFs characteristic of observers with albinism. In healthy observers, MP revealed that voxels may capture the activity of multiple subpopulations RFs that sample distinct regions of the visual field. Thus, MP provides a versatile framework to visualize, analyze and model, without restrictions, the diverse RFs of cortical subpopulations in health and disease.

## 1. Introduction

Over the past decade, our understanding of human brain function, organization and plasticity has increased tremendously. An essential contribution to this success has come from the ability to characterize the receptive field (RF) properties of neurons. The first electrophysiological measurements of those receptive field properties (in monkeys and cats) showed that the visual cortex is retinotopically organized and contains multiple maps representing the visual field (Hubel et al., 1977; Hubel and Wiesel, 1974a, 1974b). The development of non-invasive neuroimaging techniques, such as fMRI, opened a window to study brain activity directly in humans, albeit at a somewhat coarser scale. A subsequent boost to the field of visual neuroscience came from the development of

biologically plausible computational models, which enable detailed characterization, also in humans, of the collective stimulus-referred RF of a population of neurons (Dumoulin and Wandell, 2008). Such detailed characterization is essential for linking brain function and behaviour and understanding brain plasticity (for reviews, see e.g. (Dumoulin and Knapen, 2018; Haak et al., 2012; Wandell and Smirnakis, 2009)). In recent years, the approach has been extended towards neural-referred pRFs (Haak et al., 2013) and other perceptual domains, such as audition and numerosity (Harvey et al., 2015; Thomas et al., 2015).

Briefly, conventional population RF (pRF) mapping employs biologically inspired models to predict the neural tuning profiles per voxel, by systematically stimulating well defined portions of the visual field while recording the stimulus evoked activity using fMRI. Given that a standard

\* Corresponding author. Laboratory of Experimental Ophthalmology, University Medical Center Groningen, University of Groningen, P.O. Box 196, 9700, AD, Groningen, the Netherlands.

E-mail address: [j.c.de.oliveira.carvalho@rug.nl](mailto:j.c.de.oliveira.carvalho@rug.nl) (J. Carvalho).

<https://doi.org/10.1016/j.neuroimage.2019.116423>

Received 9 August 2019; Received in revised form 22 November 2019; Accepted 29 November 2019

Available online 4 December 2019

1053-8119/© 2019 Published by Elsevier Inc. This is an open access article under the CC BY-NC-ND license (<http://creativecommons.org/licenses/by-nc-nd/4.0/>).

voxel of (3 mm<sup>3</sup>) captures the cumulative activity of ~1 millions of neurons, a pRF assesses the aggregate response across all neuronal subpopulations present within a voxel and thus primarily represents the most vigorously responding subpopulation. The standard approach requires making *a priori* assumptions about the spatial, temporal and feature-selective properties of the pRF. For example, the number of pRFs per voxel is often assumed to be one and the pRF is assumed to be circular symmetric. However, such assumptions limit the ability to reveal unexpected pRF shapes, properties and subpopulations. To advance our understanding of visual processing and cortical organization, approaches that can capture more fine-grained properties of distinctive subpopulations would be required. In particular, characterization of the shape of RFs may reveal its selectivity and specificity (Chapin, 1986; DeValois, 1982; Finlay et al., 1976; Merkel et al., 2018; Ringach, 2002; Silson et al., 2018a). An example of a model that results in a detailed characterization of the RF structure is the single unit receptive field (suRF). By modelling the neuronal activity with Gabor functions, suRF enables estimation of the size of an average single-neuron RF (Keliris et al., 2019).

An analytical model that makes minimal *a priori* assumptions – enabling advanced pRF-mapping techniques – could be used to study visual pathologies, which are often characterized by highly atypical cortical pRF shapes. In such conditions, asymmetrical or even fragmented pRFs can arise that severely challenge both conventional retinotopic and contemporary pRF mapping techniques (Baseler et al., 2011; Papanikolaou et al., 2014). Such conditions could be an important application of advanced mapping techniques. While atypical and even unexpected pRFs may arise in deafferented visual cortex due to retinal or cortical lesions, very systematic deviations have been found in congenital visual pathway abnormalities (Hoffmann and Dumoulin, 2015). In albinism, for example, the visual cortex receives input from both hemifields, resulting in voxels with bilateral pRFs in opposing visual hemifields (Hoffmann et al., 2003; Kaule et al., 2014). These pRFs are associated with an erroneous projection of the axons from the temporal retina to the contralateral hemisphere, which affects the central vertical portion of the visual field. Due to the predictability of the resulting pRF-abnormalities, i.e. their bilaterally split shape, albinism is ideal for validating the performance of new pRF-mapping techniques that have been optimised – with minimal *a priori* assumptions – to reveal highly atypical pRFs.

We therefore developed a technique for capturing the activity and properties of neuronal populations and subpopulations, which we present here. This approach efficiently samples the entire stimulus space, such as the visual field, with a “micro-probe”: a 2D Gaussian with a small standard deviation. Regions of stimulus space that exhibit better model fits will be more heavily sampled. Like the conventional pRF approach, these micro-probes sample the aggregate response of neuronal populations, but they do so at a much higher level of detail. Consequently, for each voxel, the MP generates a probe map representing the density and variance explained (VE) for all the probes. The probe maps are visual field coverage maps that can be used for visual inspection and for directly deriving neural properties such as symmetry. Moreover, following probe thresholding and clustering, they can also be used for identifying multiple clusters within a voxel. We define a cluster as an aggregate of probes, that together have a distinct position, shape and size). Such cluster properties can be characterized by fitting shape models, if desired. Biologically, a cluster can be interpreted as a (sub-) population of RFs. When it is necessary to distinguish a population RF identified using MP, we will refer to it as a pRF<sub>mp</sub>.

A primary advantage of our new approach is that it makes minimal *a priori* assumptions about the pRF properties or the number of constituent clusters. For example, there is no need to specify up front the expected number of spatial locations that a recording site (voxel) may respond to. We validated and tested the limits and capabilities of our new method using both in-vivo visual field mapping data and simulations. Without using specific stimuli or models, we recovered bilateral receptive fields in primary visual areas that are typical for the abnormal visual field

representations in albinism (Hoffmann et al., 2012, 2003). Moreover, to demonstrate its versatility, we empirically estimated multiple clusters properties in healthy participants within a pRF<sub>mp</sub>.

## 2. Materials and methods

The methods are presented in the following order. First, we will go through the steps of the MP framework. Second, we will describe the acquisition procedure. Third, we will describe how the MP analysis is applied to simulations, empirically acquired fMRI data from healthy observers, and to the fMRI data of a cohort of observers with albinism and age-matched controls.

### 2.1. Micro-probing framework

To describe the MP framework, we first recapitulate the conventional pRF approach on which MP is based. Second, we describe the application of a Bayesian Markov Chain Monte Carlo (MCMC) sampling approach (see (Adaszewski et al., 2018)) which results in a probe map. Note that the MCMC approach is not crucial for MP, but significantly reduces the computational requirements by efficiently sampling the entire stimulus space. Finally, we describe how we derive the pRF<sub>mp</sub> characteristics. The framework is shown in Fig. 1.

#### 2.1.1. Probe definition and conventional pRF fitting procedure

The core of MP is based on the conventional pRF method (Dumoulin and Wandell, 2008). Similar to the conventional pRF, a probe is defined as a 2D Gaussian in Cartesian coordinates (in deg) in visual space, centered at  $\hat{x}$  and  $\hat{y}$ . However, in our MP we force a narrow fixed width ( $\sigma$ ). The results shown in this study were obtained with  $\sigma = 0.01$ deg.

$$probe = e^{\frac{-(x-\hat{x})^2 + (y-\hat{y})^2}{-2\sigma^2}} \quad (1)$$

As in the conventional pRF approach, we predicted the voxel's response to the stimulus  $p(t)$  by calculating the overlap between the stimulus and the probe at each time point  $s(x, y, t)$ :

$$p(t) = \sum_{x,y} s(x, y, t) * probe(x, y) \quad (2)$$

Second, we accounted for the delay in the hemodynamic response by convolving  $p(t)$  with the hemodynamic response function (Boynton et al., 1996; Friston, 1998). Finally, assuming a linear relation between the predictor and the fMRI response, we minimized the error per time point,  $e_t$  using ordinary least squares. In order to facilitate the MCMC procedure, a likelihood ( $l$ ) is calculated, based on this  $e_t$  as follows:

$$l_t = \log(N(-|e_t|, \hat{\mu}, \hat{\sigma}) \rho, \theta) \quad (3)$$

Here, we assumed that  $e_t$  is normally distributed, enabling the estimation of the mean and standard deviation ( $\hat{\mu}$  and  $\hat{\sigma}$ , respectively). Given  $\hat{\mu}$  and  $\hat{\sigma}$ , we calculated the total likelihood,  $L$ , accounting for the contribution of the priors of  $\rho$  and  $\theta$ .

$$L = \sum_t (l_t) + \log(prior_\theta) + \log(prior_\rho) \quad (4)$$

#### 2.1.2. Bayesian MCMC

In order to obtain (per voxel) a projection in stimulus space of all the probes weighted by their VE (probe map), probes were fitted at different locations. To this end, the MCMC approach was implemented to efficiently sample the entire visual field. The center of the probe was defined using two latent variables. We used the nomenclature of Zeidman and colleagues (2018). Let  $l_\rho$ ,  $l_\theta$  be the latent variables corresponding to the radius and angle of the pRF center, respectively. The probe position of a RF in polar coordinates is given by:

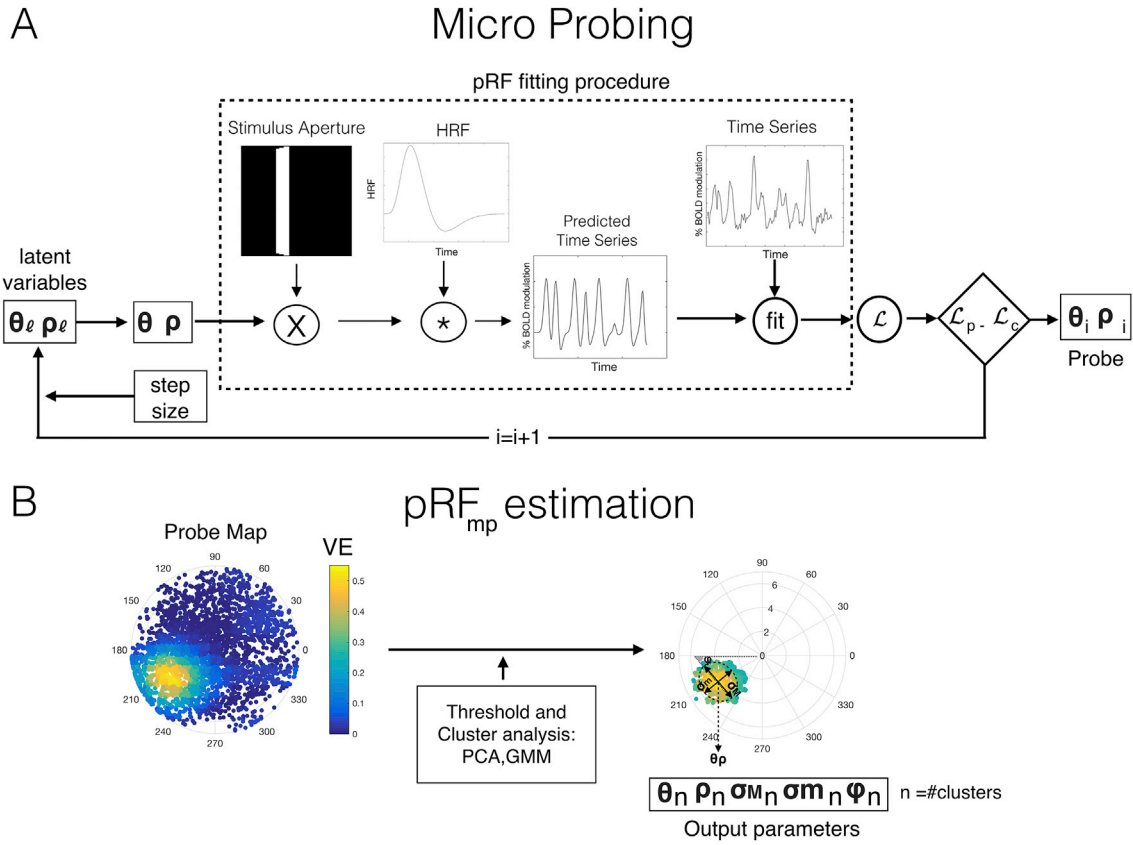


**Fig. 1. Overview of the micro-probing framework.** Panel A: MP: MCMC procedure from the latent variables to the probes, including the fitting procedure partly based on the conventional pRF approach (Dumoulin and Wandell, 2008). Note that a probe map is composed by every probe ( $\theta_i, p_i$ ) weighted by its respective VE. Panel B: pRF<sub>mp</sub> estimation based on the probe map: this step includes thresholding the probes such that only the most explanatory ones are retained followed by cluster analysis. The output parameters are: the number of clusters within a pRFs<sub>mp</sub> ( $n$ ); the position of the pRFs<sub>mp</sub> (clusters), eccentricity ( $\rho$ ) and polar angle ( $\theta$ ); the size of the pRF<sub>mp</sub> (clusters) which is defined based on the major and minor axes of the ellipse  $\sigma_m$  and  $\sigma_n$ , respectively and the orientation of the pRF<sub>mp</sub> ( $\phi$ ).

$$\rho = r * NCDF(l_\rho, 0, 1) \quad (5)$$

$$\theta = 2\pi * NCDF(l_\theta, 0, 1) - \pi \quad (6)$$

Here  $r$  is the radius of the stimulated visual field, in degrees.  $NCDF$  is the normal cumulative density function. Note that the center of the probe was constrained to fall within the stimulated visual field. As the MP fitting procedure was done in Cartesian coordinates, the polar coordinates were converted as follows:

$$x = \rho * \cos(\theta) \quad (7)$$

$$y = \rho * \sin(\theta) \quad (8)$$

To incorporate biological prior knowledge about the expected distribution of the probes within the visual field, a prior was assigned to each of the latent variables,  $l_\theta$  and  $l_\rho$ . Based on (Zeidman et al., 2018), these priors were defined as normal distributions,  $N(0,1)$  which, after conversion into polar coordinates ( $\rho$  and  $\theta$ , equations (5) and (6)), express the assumption that the density of neurons is higher in the fovea than in the periphery (Azzopardi and Cowey, 1993). In this study, we initialized  $l_\rho$ ,  $l_\theta$  with 0.5 and 1, respectively.

In the Bayesian MCMC procedure two probe locations are compared, the current probe and the proposal (new probe), these are indicated by a  $p$  and  $c$  in Fig. 1. The position of the proposal probe is based on the current one as follows: the step size was controlled by  $d_{proposal}$ . In this study we defined  $\mu_d$  and  $\sigma_d$  as 0.5 and 2, respectively.

$$d_{proposal} = |N(\mu_d, \sigma_d)| \quad (9)$$

$$l_\rho \text{ proposal} = N(l_\rho \text{ current}, d_{proposal}) \quad (10)$$

$$l_\theta \text{ proposal} = N(l_\theta \text{ current}, d_{proposal}) \quad (11)$$

To evaluate whether the current position will be updated by the proposal position, the following steps were used in a MCMC approach. The likelihood of the proposal probe was compared to that of the current probe. Therefore, an acceptance ratio,  $Ar$ , was computed.

$$Ar = e^{(\mathcal{L}_p - \mathcal{L}_c)} \quad (12)$$

This was used as follows. If  $Ar$  is bigger than one, the proposed probe results in a better fit than the current one, and the current position is updated. If  $Ar$  is smaller than one, the fit is not better, yet there is still a chance to update the current position. For this, a probability of random acceptance,  $accept$  was defined as  $N(0,1)$ . If  $Ar$  is bigger than  $accept$ , the latent variables  $l_\rho$ ,  $l_\theta$  are updated nevertheless.

To ensure that the entire visual field is probed, 12 different starting positions (equally distributed over the search grid) were defined. Per voxel, a total of 10,000 iterations (~833 per starting position) took place. This minimized the risk of local minima, i.e. oversampling a specific pRF<sub>mp</sub>. The combined results of all 10,000 current probe locations (position, variance explained) comprise the basis for the probe map of a particular voxel.

### 2.1.3. Estimation of pRFs using MP

Following the iterations, we generated a probe map consisting of the projection in the stimulus space of all the probes weighted by their VE. Note that a visual inspection of this probe map already informs about the properties of the neural (sub-) population(s) that are present in the voxel.

In addition, based on this probe map, we can estimate various pRFs properties, such as the number of clusters, position, size, elongation, orientation, and irregularity of the shape and VE (Fig. 1B).

The pRF<sub>mp</sub> estimation comprises three steps: first, we select the k% probes with the strongest VE (k-threshold). Additionally, these probes need to have a VE above VEmax - VEr. Where VEmax is VE of the best fitting probe and VEr defines the VE range. We found this additional selection improves any subsequent clustering and shape estimation. Unless specified otherwise, in the present study we used a value of 15% and 0.1 for k and VEr, respectively.

Second, the number of clusters in the pRF<sub>mp</sub> was determined by applying a weighted cluster analysis. Gap statistics were used to evaluate whether a single or multiple clusters were present (Tibshirani et al., 2001). In the latter case, to estimate the number of clusters, the Davies-Bouldin index clustering (DB) algorithm was applied (Davies and Bouldin, 1979). Note that the particular choice of the clustering algorithm does not critically affect the number of estimated clusters (Fig. S3). The maximum number of clusters that can be estimated needs to be defined *a priori*. In this study, we defined a maximum of four clusters for simulations and healthy observers and eight in case of observers with albinism and their aged-matched controls.

Third, the properties of the individual clusters in the pRF<sub>mp</sub> were determined using a Gaussian mixture model. This probabilistic model assumes that all data points were generated from a mixture of a finite number of Gaussians distributions with unknown parameters. The number of Gaussians to fit corresponds to the number of clusters calculated in step 2. Furthermore, this model enables detection of the presence of a subpopulation within an overall population without requiring *a priori* identification of the subpopulation to which an individual probe belongs.

To determine how strongly the estimated pRF<sub>mp</sub> characteristics depend on the choice of clustering algorithm, we applied two additional clustering algorithms, the Silhouette (S) and CalinskiHarabasz (CH), to the simulated and empirical data.

The code for MP is available via:

<https://www.visualneuroscience.nl/tools/>.

## 2.2. Simulations

To verify the precision of our model, we simulated multiple pRFs within a voxel using the conventional pRF model. These were centered at multiple locations and had different sizes and shapes (elongation and orientation). The simulation of elongated pRF shapes according to different orientations was done using an ellipsoidal Gaussian model, defined as follows:

$$a = \frac{\cos(\varphi)^2}{2\sigma_M^2} + \frac{\sin(\varphi)^2}{2\sigma_m^2} \quad (13)$$

$$b = \frac{-\sin(2\varphi)}{4\sigma_M^2} + \frac{\sin(2\varphi)}{4\sigma_m^2} \quad (14)$$

$$c = \frac{\sin(\varphi)^2}{2\sigma_M^2} + \frac{\cos(\varphi)^2}{2\sigma_m^2} \quad (15)$$

$$pRF_{ellipsoidal} = e^{-a(x-x_0)^2 - 2b(x-x_0)(y-y_0) + c(y-y_0)^2} \quad (16)$$

where  $\sigma_M$  and  $\sigma_m$  are the major and minor axes of the ellipse, respectively.  $\varphi$  represents the angle between the major axis and the horizontal meridian. Note that formulas 13–15 define the coefficients  $a$ ,  $b$  and  $c$  used in formula 16.

The total profile was given by the sum of the simulated individual pRFs. Next, the simulated time series were calculated based on the steps to generate the predicted times series (equation (2)). We used the standard moving bar stimuli, described in the stimulus section. White Gaussian noise was added to the simulated time series.

$$pn(t) = p(t) + n \quad (17)$$

$$var = 10^{-\frac{SNR}{10}} \quad (18)$$

$$n = \sqrt{var} * N \quad (19)$$

where  $pn(t)$  is the predicted time series with added noise,  $p(t)$  is the predicted time series and  $n$  is the white gaussian noise, while  $var$  is the variance of the noise.

Additional simulations used to test the effect of the k-threshold and the reliability of the estimated pRF<sub>mp</sub> are described in the supplementary material (Figures S1, S2 and S3).

## 2.3. Empirical studies

### 2.3.1. Participants and ethics statement

We recruited 7 participants (3 females; average age: 28; age-range: 26–32 years-old) with normal or corrected to normal vision. Prior to scanning, participants signed an informed consent form. Our study was approved by the University Medical Center of Groningen, Medical Ethical Committee and conducted in accordance with the Declaration of Helsinki.

### 2.3.2. Data acquisition

Stimuli were presented on an MR compatible display screen (BOLDscreen 24 LCD; Cambridge Research Systems, Cambridge, UK). The screen was located at the head end of the MRI scanner. Participants viewed the screen through a tilted mirror attached to the head coil. Distance from the observer's eyes to the display (measured through the mirror) was 120 cm. Screen size was  $22 \times 14^\circ$ . The maximum stimulus radius was  $7^\circ$  of visual angle. Visual stimuli were created using MATLAB and the Psychtoolbox (Brainard, 1997; Pelli, 1997).

### 2.3.3. Experimental procedure

Each participant participated in one (f)MRI session. Retinotopic mapping was done using a standard drifting bar aperture defined by high contrast-inverting checkerboard texture (Dumoulin and Wandell, 2008). The contrast inverted at a frequency of 8 Hz and the size of the inner bar was  $0.55^\circ$ . The bar aperture moved in 8 different directions (4 bar orientations: horizontal, vertical and the two diagonal orientations, with two opposite drift directions for each orientation). The bar moved across the screen in 16 equally spaced steps each lasting 1 TR. The bar contrast, width and spatial frequency were 100%, 1.75 and 0.5 cycles per degree, respectively. After 24 steps (one pass and a half), 12 s of a blank full screen stimulus at mean luminance was presented.

A single retinotopic mapping run consisted of 136 functional images (duration of 204 s). Eight prescan images (duration of 12 s) were discarded. During scanning, participants were required to perform a fixation task in which they had to press a button each time the fixation point turned from green to red. The average (std. err) performance on this task was 90.9% ( $\pm 6.8\%$ ).

### 2.3.4. MRI scanning and fMRI data processing

Scanning was carried out on a 3 T S Prisma MR-scanner using a 64-channel receiving head coil. A T1-weighted scan (voxel size,  $1 \text{ mm}^3$ ; matrix size,  $256 \times 256 \times 256$ ) covering the whole-brain was recorded to chart each participant's cortical anatomy. The functional scans were collected using standard EPI sequence (TR: 1500 ms; TE: 30 ms; voxel size of 3 mm isotropic, flip angle of 80 and a matrix size of  $84 \times 84 \times 24$ ). The T1-weighted whole-brain anatomical images were re-sampled to a  $1 \text{ mm}^3$  resolution. The resulting anatomical image was automatically segmented using Freesurfer (Dale et al., 1999). The cortical surface was reconstructed at the gray/white matter boundary and rendered on an inflated and smoothed 3D mesh (Wandell et al., 2000).

The functional scans were analysed in the mrVista software package



for MATLAB (available at <http://white.stanford.edu/software>). Head movement artefacts between and within functional scans were corrected (Nestares and Heeger, 2000). The functional scans were then averaged and coregistered to the anatomical scan (Nestares and Heeger, 2000) and interpolated to the anatomical segmentation. For comparison, the data was also analysed with conventional pRF modelling (Dumoulin and Wandell, 2008). A 2D-gaussian model was fitted with parameters  $x_0$ ,  $y_0$ , and  $\sigma$  where  $x_0$  and  $y_0$  are the receptive field center coordinates and  $\sigma$  is the spread (width) of the Gaussian signal, which is also the pRF size. We used SPM's canonical difference of gammas for the HRF model. All parameter units are in degrees of visual angle and stimulus-referred. The borders of visual areas were determined on the basis of phase reversal (phase as obtained with the conventional pRF model). For each observer, six visual areas (V1, V2, V3, V4, LO1 and LO2) were manually delineated on the inflated cortical surface.

### 2.3.5. Test-retest analysis

The accuracy and robustness to noise were investigated by a test-retest analysis. For this, the data was divided in two test sets (three odd runs and three even runs). MP was performed on each set. Subsequently, each probe map was converted into a heat map for each voxel by calculating the average VE per bin with a resolution of  $40 \times 40$ . Following this the correlation coefficient between the two heat maps was computed. The reproducibility for a given region was evaluated by inspecting the histogram across all voxels.

### 2.3.6. Participants with albinism

Analysis was performed using both conventional pRF modelling and our new MP approach. In the case of conventional pRF modelling, three models were used: a standard single Gaussian model and two bilateral Gaussian models, the latter two with positions that were symmetric in either the vertical or the horizontal axis. Three visual areas (V1 and V2 and V3) were defined in the left and right hemisphere of each observer. In observers A01 and A02, we could define V1 only in the right hemisphere due to too much noise in the phase maps.

The data of the healthy and albinism observers is available at XNAT central under the project ID: fMRI\_micro\_probing.

### 2.3.7. Symmetry analysis of probe maps

For analysing the data of the observers with albinism, an additional symmetry analysis was developed based on the probe maps to quantify the degree of symmetry in the pRF<sub>mp</sub> estimated for a voxel. This provides an indication of the degree to which visual information is misrouted. This analysis comprised three steps: 1) convert the probe map (Fig. 2A) into a heat map with a resolution of  $40 \times 40$  bins (Fig. 2B); 2) flip this "image" across the eight axes from 0 to 180° in steps of 22.5°, and 3) compute the correlation coefficient between the original and transformed (flipped) images. This resulted in correlation coefficients that indicate the extent to which the images are completely asymmetrical (0) or identical (1).

Fig. 2 depicts the symmetry estimation procedure for a typical voxel of an albinism observer. The degree of similarity between the original

and mirrored image was translated into a correlation coefficient. By computing the symmetry coefficient in each probe map over the early visual cortex we identified regions that received input from both the contralateral and ipsilateral visual field.

## 3. Results

### 3.1. MP validation using simulations

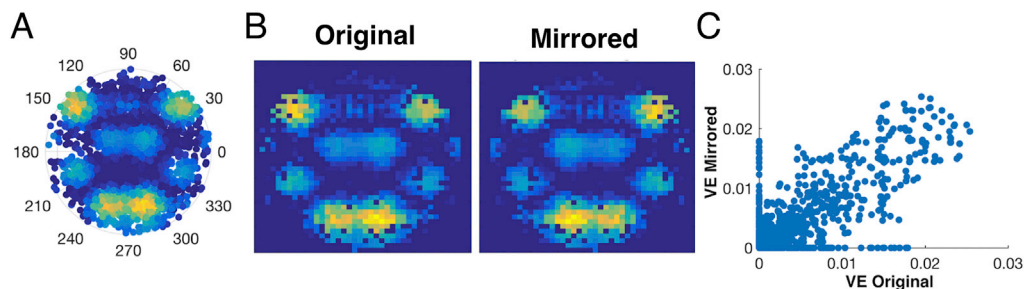
#### 3.1.1. Detection of different shapes and robustness to noise

Fig. 3 shows the result of MP for a single simulated bilateral pRF mirrored to the vertical meridian. The probes were positioned at  $[3.5, 3.5; -3.5, -3.5]$  and the probes had different shapes. The one positioned in the positive quadrant was ellipsoidal (major axis,  $\sigma_M = 1.7$  deg, and minor axis,  $\sigma_m = 1.2$  deg, with an orientation of 45 deg) and other was circular symmetric ( $\sigma = 1$ ). Note that probes with the simulated pRFs present a higher variance explained than the remaining visual field. After thresholding the probe maps, the two simulated pRFs were recovered (panel B). Panel C compares time series as predicted by MP (red) and the conventional ellipsoidal pRF (blue). Despite the artificial noise added, MP well-captured the dynamics of the simulated time series, and fitted the simulated data better than the conventional pRF. Moreover, MP could accurately detect the number of clusters in the pRFs as well as their shape.

Additionally in SI we showed: 1) how the pRF<sub>mp</sub> characteristics were affected by the k-threshold. A stringent k-threshold minimized the eccentricity error, while more lenient ones minimize the size error (Fig. S1). Note that the eccentricity and size error corresponded to absolute difference between eccentricity and size estimated using MP and the eccentricity and size of the simulated pRF (ground truth). Polar angle estimates were not influenced by the k-threshold. 2) MP is highly robust to noise and accurately determines the number of simulated pRFs (or clusters) per voxel as well as their position and shape (Fig. S2). 3) The choice of the algorithm did not significantly influence the number of clusters detected within a voxel. On average 80% and 75% of the times the three algorithms tested (including DB) detected the same number of clusters in the simulated and empirical data (Fig. S3). 4) MP better detected the shape of the pRF than the conventional method (using an ellipsoidal model), resulting in lower elongation and orientation error (Fig. S4), importantly these simulations were obtained for single pRFs. 5) We showed which parameters may affect the pRF<sub>mp</sub> performance. The main factors affecting the accuracy of MP were the actual number of simulated pRFs (or clusters) within a voxel and their proximity (Fig. S5). Notably the closer the clusters, the more difficult it is to distinguish them. Hence, their activity will be aggregated resulting in an underestimation of the number of clusters. The larger the number of clusters, the higher the probability of errors in the estimation of their number and size.

### 3.2. Retinotopic mapping using MP

We applied MP to the retinotopic mapping data of healthy observers.



**Fig. 2.** Calculation of a symmetry coefficient based on a probe map. A: Probe map of a typical V1-voxel of observer with albinism A01. B: Original and mirror images to the vertical meridian reconstructed. C: VE per bin of the mirrored image as a function of the original image, for one representative voxel in V1. The symmetry coefficient of this particular voxel is 0.8.

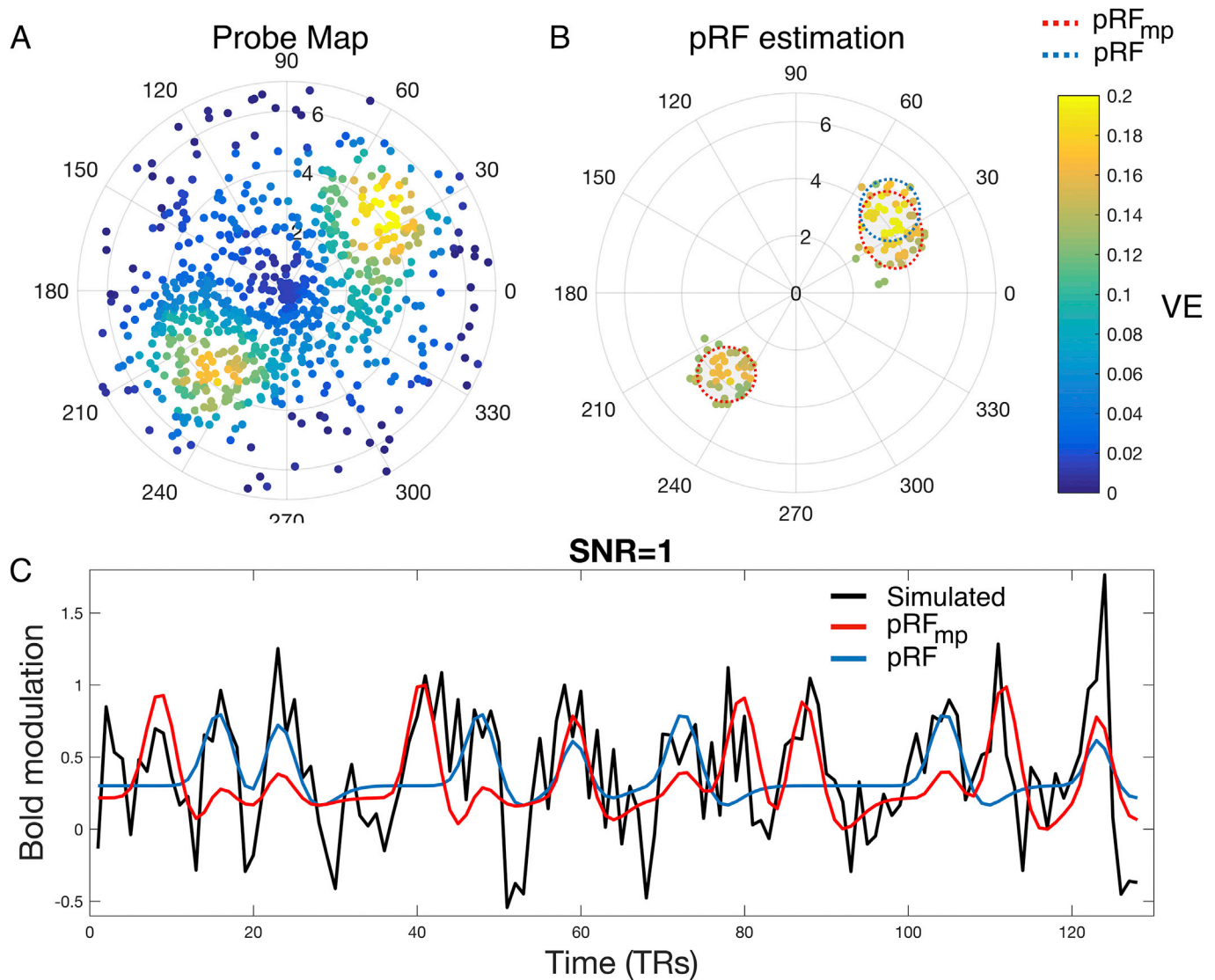


**Fig. 3. Micro-probing simulated bilateral pRFs with different shapes.** Panel A: probe map obtained from the simulated time series. The colour bar represent the variance explained. Panel B: Thresholded probe map, using a  $k$  threshold of 15% and the results of the clustering and Gaussian mixture model analysis. The estimated pRF<sub>mp</sub> and pRF are indicated by the shaded gray gaussians, outlined in red and blue respectively. Panel C: Simulated time series of bilateral pRFs (black) and the predicted time series estimated with conventional pRF (blue) and with MP (red), using a SNR of 1. The predicted time series estimated on the basis of MP was calculated using the estimated pRF<sub>mp</sub> clusters.

Fig. 4 shows two examples of probe maps for three representative V1 voxels and the derived pRF<sub>mp</sub> properties. It shows the estimated pRFs<sub>mp</sub> at various  $k$ -thresholds (which sets the percentage of probes with the strongest VE included in the pRF<sub>mp</sub> estimation) and compares these to the conventional pRF estimates.

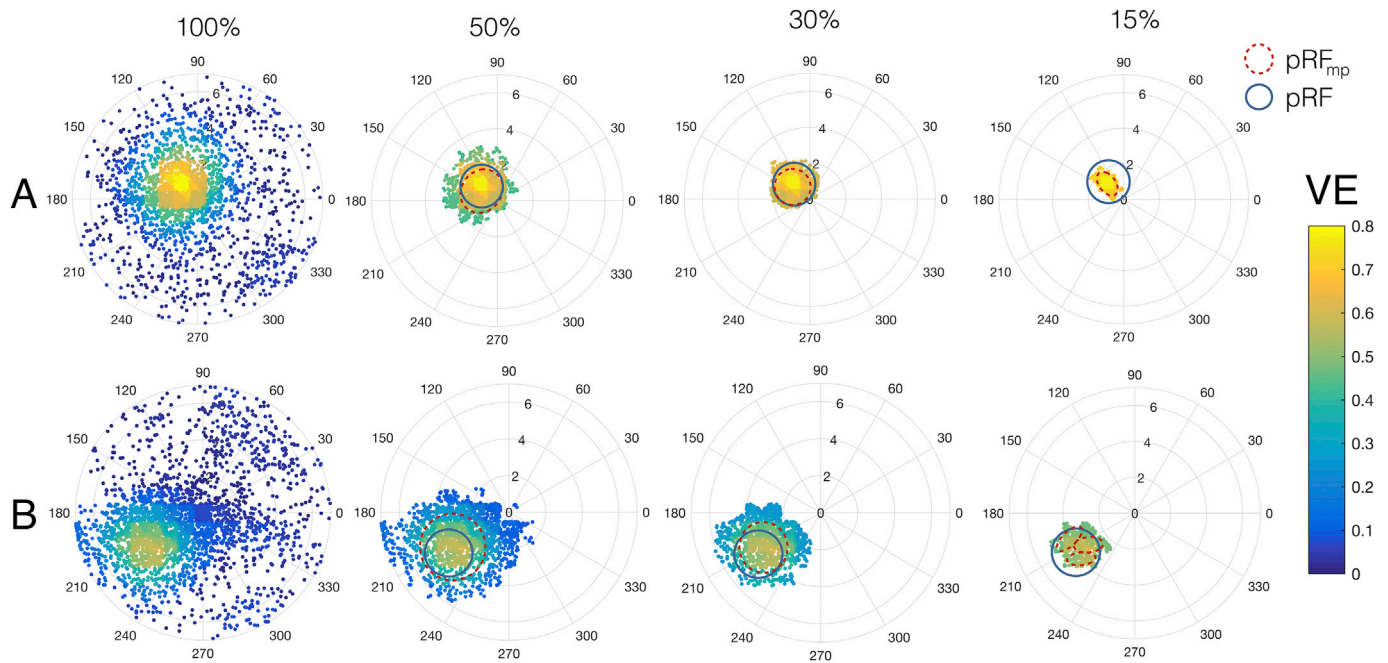
Fig. 4 indicates various features of the MP approach. First, it shows that the estimated size of the pRF<sub>mp</sub> depends on the chosen  $k$ -threshold. Please note that the location of the pRF<sub>mp</sub> does not depend on the chosen threshold. A more stringent threshold also enables identification of multiple clusters (Fig. 4B). More liberal thresholds result in pRF<sub>mp</sub> that are approximately similar in size to conventional pRFs, whereas more stringent thresholds result in smaller pRF<sub>mp</sub> (Fig. 4A).

Fig. 5A depicts the similarity of the eccentricity maps obtained with the conventional pRF and MP approaches. Fig. 5D shows that the pRF<sub>mp</sub> and conventional pRF eccentricity are highly correlated. In the periphery, however, the estimated pRF<sub>mp</sub> have somewhat lower eccentricity (i.e. they are situated more foveally) than the accompanying pRFs. This is particularly noticeable for higher-order areas.

Fig. 5B shows the projections of pRF and pRF<sub>mp</sub> size on an inflated

brain mesh. Due to our choice of  $k$ -threshold (15%) and a  $VE_r$  (maximum difference in VE between the most and least explanatory probe) of 0.1, the pRFs<sub>mp</sub> sizes shown here are significantly smaller than those of the conventional pRFs (note the different scales). Nevertheless, Fig. 5E shows that both pRF and pRF<sub>mp</sub> size increase with eccentricity, irrespective of the  $k$ -threshold used. Note how the choice of  $k$ -threshold influences the estimated pRF<sub>mp</sub> size. The less stringent the  $k$  and/or  $VE_r$  threshold, the higher the number of probes, with lower explanatory value, taken into consideration. As expected, the higher the number of probes taken into account the larger the pRF<sub>mp</sub> size. These thresholds restrict the restrictiveness of the pRF<sub>mp</sub> definitions. In other words, these thresholds restrict the susceptibility of the method to noisy data. Nonetheless, the size of the pRFs<sub>mp</sub> can be compared across, e.g. eccentricity, visual areas or observers, given a choice for  $k$  and  $VE_r$ .

Fig. 5C shows (projected on an inflated brain mesh) the close similarity of the VE for pRF and pRF<sub>mp</sub> model estimates. Fig. 5F shows that voxels for which the classic pRF method yielded low VE ( $VE < 0.1$ ) were better described by MP (higher VE), whereas voxels with high VE in conventional pRF modelling ( $VE > 0.8$ ) were actually characterized



**Fig. 4. Examples of MP probe maps.** Also shown are comparison of MP derived pRFs and conventional pRF estimations for V1 voxels. Shown are results obtained for three V1 voxels and with probe maps thresholded at a k-threshold of 100%, 50%, 30% and 15% (this k-threshold determines the percentage of probes with best VE included in the pRF<sub>mp</sub> estimation). It is clear that the conventional pRF (blue circles) and MP-based pRF estimates (dashed red outlines) can differ in various ways: A) estimated pRF<sub>mp</sub> size and shape depend on k-threshold. B) At lenient k-thresholds (100%, 50%, 30%), MP revealed a single cluster, while at a more stringent threshold it detected multiple clusters. Data was obtained during retinotopic mapping. The V1 voxels were extracted from the right hemisphere of observer S07.

worse by MP. This is partly because the conventional pRF method tends to estimate larger pRFs, which also results in a higher VE. Fig. S8 shows that increasing the k-threshold for MP also increases the estimated pRF<sub>mp</sub> size, resulting in a higher VE.

### 3.3. MP reliability: test-retest analysis

Fig. 6 shows that the probe maps obtained with the test set were similar to the ones obtained with the retest set (Fig. 6A and B). Fig. 6C shows that for the majority of the voxels there was a good agreement (high correlation coefficient) between the results obtained with the test and retest dataset. Moreover voxels whose correlation between the probe maps obtained using both datasets was below 70% were associated with very noise signals, i.e. the maximal VE was below 0.2.

### 3.4. Application of MP in albinism

To demonstrate the biological relevance of our new technique, we applied MP to data obtained in observers with albinism. Based on previous work in observers with albinism, we expected to find mirror symmetry in the positions of the estimated pRF<sub>mp</sub> clusters with respect to the vertical meridian (Hoffmann et al., 2012, 2003; Kaule et al., 2014). Fig. 7A shows the projection of the symmetry coefficients (calculated based on the probe maps regarding the vertical midline) onto the reconstructed hemispheres of a representative observer with albinism and a control observer. See method section “Symmetry analysis of probe maps” for more details. In albinism, the probe maps revealed a large number of voxels with pRFs<sub>mp</sub> that were mirrored across the vertical meridian. Closer inspection of the probe map of Fig. 7C, showed highly symmetrical and spatially organized pRF<sub>mp</sub> in an example voxel. The cortical projections showed that most of the symmetry coefficients were much higher in albinism than in the control observer, and that neighbouring voxels had similar symmetry coefficients. Central regions showed higher symmetry coefficients than peripheral ones. Moreover, we found that a clear overlap between the cortical region with high

symmetry values and the right-left hemifield overlap cortical region (dashed line) that was determined based on stimulating the left and right hemifield in separate experiments (described in (Ahmadi et al., 2019)). In control observers, high symmetry values were found for voxels with a pRF<sub>mp</sub> near the border of visual areas (e.g. V1/V2), where the pRF<sub>mp</sub> is expected to be located on or very close to the vertical meridian. Fig. 7B illustrates why such voxels also have high symmetry coefficients.

To demonstrate the versatility of MP, Fig. 8A shows the symmetry calculated for a series of symmetry axes for the V1 region of the right hemisphere of every observer during full field stimulation. Controls had slightly increased symmetry coefficients for both the horizontal and vertical symmetry axes (0 and 90°). This reflects the symmetry of neuronal populations located along the vertical and horizontal meridians and the distribution of pRFs in the visual field. Fig. S11 shows the high number of pRFs<sub>mp</sub> located on the horizontal meridian. For observers with albinism, the inter-observer variability corresponded with their differing levels of misrouting. As expected, those with severe misrouting (top row) showed a high degree of symmetry for the vertical axis. No systematic differences were found for albinism observers with low levels of misrouting (bottom row). Fig. 8B shows that patients with a clinically established high level of misrouting had much higher V1 symmetry coefficients for the vertical axis. The symmetry coefficient to the vertical meridian is thus indicative of misrouting.

### 3.5. Using MP to estimate pRF properties

Using MP, it is relatively straightforward to explore a variety of pRF<sub>mp</sub> properties, such as the number of clusters per voxel, pRF bilaterality or pRF shape (e.g. elongation). Fig. 9A shows a map of the spatial organization of the number of pRFs<sub>mp</sub> clusters over the visual cortex, projected on the inflated right hemisphere of a representative observer. Neighbouring voxels tend to have a similar number of clusters. Comparable results were also observed in observers with albinism (Fig. S12A). Closer inspection of the probe map of a single voxel (9B) shows how MP resolves multiple clusters and their corresponding properties. Fig. 9C shows how



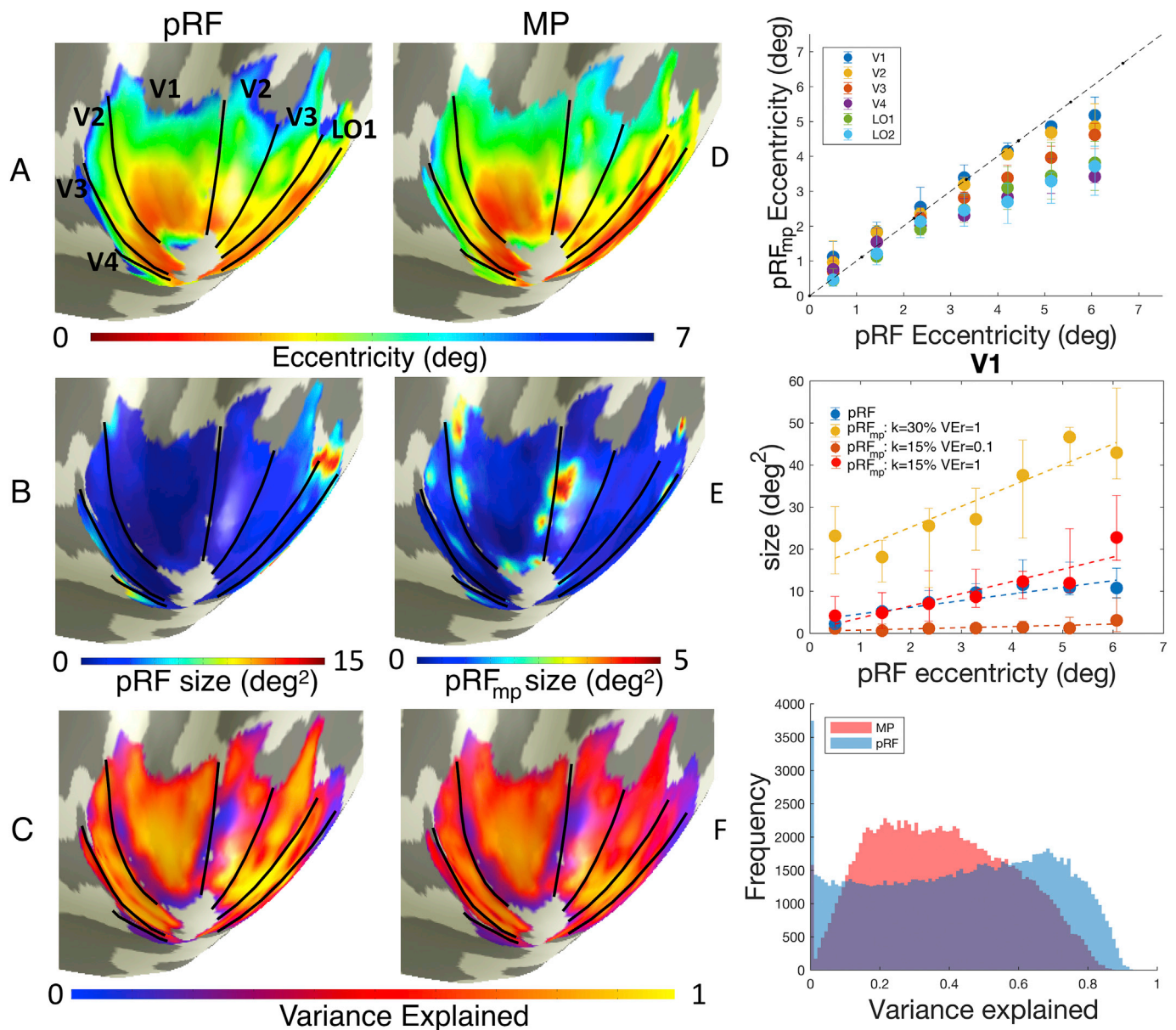


**Fig. 5. Comparison of MP-derived pRF and conventional pRF estimates.** Panel A: pRF and pRF<sub>mp</sub> eccentricity maps projected on an inflated brain mesh. If MP identified multiple clusters for a voxel, the eccentricity map shows the eccentricity of only one (arbitrarily chosen) cluster. Panel B: Left: pRF and pRF<sub>mp</sub> area maps projected on an inflated brain mesh. Panel C: Left: pRF and pRF<sub>mp</sub> area maps projected on an inflated brain mesh. Panel D: Median eccentricity of the clusters of pRF<sub>mp</sub> as a function of the eccentricity of the conventional pRF (the dashed line represents a perfect correlation). The pRF eccentricity was binned in 1° bins of eccentricity (data from 7 healthy observers: 14 hemispheres). Error bars represent 5% and 95% confidence intervals. For the visual areas tested, pRF<sub>mp</sub> eccentricity correlated highly with that of the corresponding conventional pRF (correlation coefficients vary between 0.98 and 1, depending on the visual areas, with p-values < 0.05; see Table S1 for the correlation values and corresponding p-values). Fig. S6 shows the relationship between the eccentricity of all clusters and the conventional pRF. Panel E: pRF<sub>mp</sub> (at different k-thresholds and VEr (VE-range)) and pRF size as a function of eccentricity. The pRF<sub>mp</sub> size of an arbitrarily chosen cluster was binned in 1° bins of eccentricity (data from 7 healthy observers: 14 hemispheres). Error bars represent 5% and 95% confidence intervals. The dashed lines represent the linear fit. Fig. S7 shows the relation between the size and eccentricity of all clusters and the 6 visual areas tested. Panel F: Histogram of the VE for pRF<sub>mp</sub> (blue) and pRFs (red). The VE was based on the cumulative activity of the number of clusters. The histogram shows the data accumulated across 6 visual areas and 7 healthy observers (14 hemispheres).

pRF<sub>mp</sub> tend to be more elongated (i.e. less spherical) in the (para-)fovea compared to the periphery. We observed this trend in all visual areas analysed (Fig. S13A). Moreover the regularity of the shape can be assessed by measuring the skewness of the distributions. V1 had predominantly regular shapes (skewness = 0). The irregularity of the shape tended to increase over the visual hierarchy (Figs. S13B and D). The kurtosis of the probe distribution was positive. This indicated that there was a high sample density at the pRF center and that the thresholding was not too severe (Figs. S13C and E). Fig. 9D shows how unilateral and

bilateral pRFs were distributed over the visual cortex, again for a representative observer. Closer inspection of the probe map of one voxel (Fig. 9E), shows how MP revealed two clusters situated in opposite hemifields and quadrants. For the vast majority of the voxels, the estimated clusters were located within the same (contralateral) hemifield (dark blue). However, some voxels contained bilateral pRFs. These are pRF<sub>mp</sub> clusters that process information from both the left and right hemifields. The bilateral pRFs appeared to be spatially organized and clustered along the vertical meridian (red blobs in Panel D). Panel F



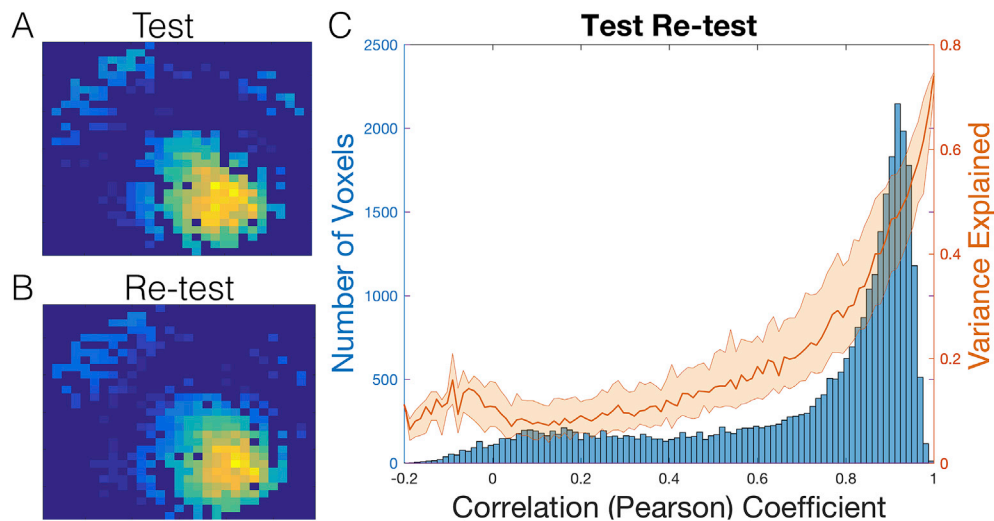


**Fig. 6. Test-retest analysis.** A and B Probe map of a V1-voxel obtained using the test and retest data set respectively. B: Histogram of the number of voxels as a function of the correlation coefficient between the test and retest probe maps of V1, overlaid with the VE obtained per bin (orange). The orange line represents the median VE and the shaded area the 25th to 75th percentile range. The histogram represents the data of the 14 hemispheres (7 observers).

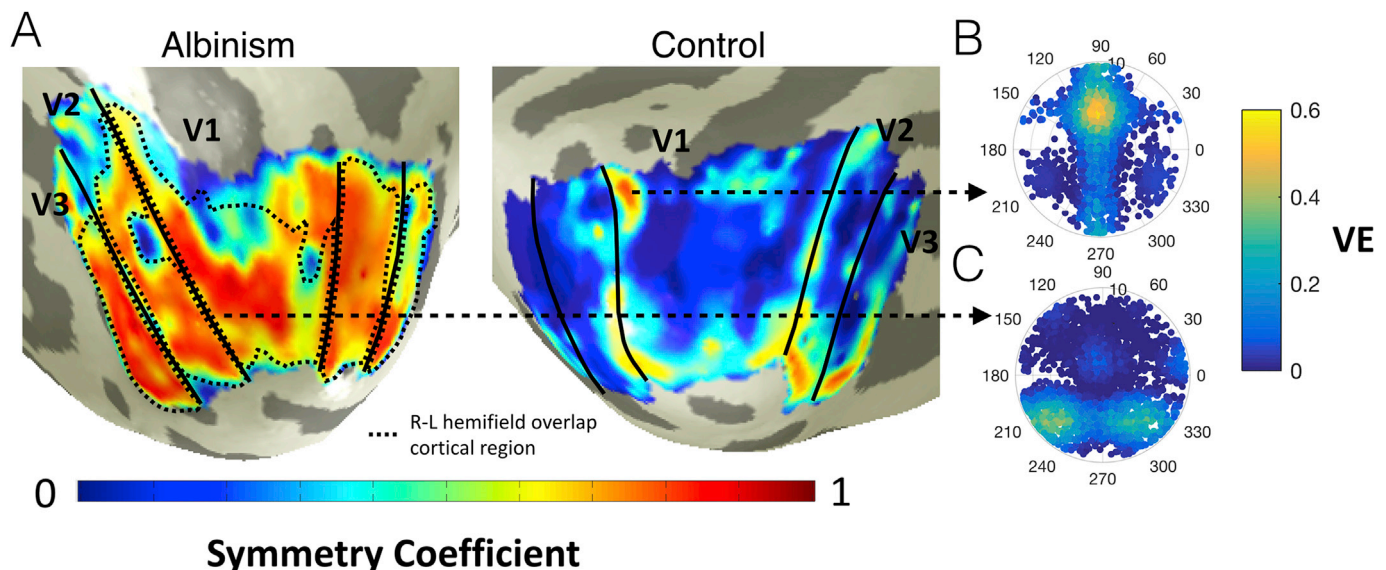


**Fig. 7. Symmetry maps in albinism and aged-matched control.** Panel A: Symmetry map for the left hemisphere of the observer with albinism A03 and of the aged match control C03. The black continuous lines outline the visual areas and the black dashed line outlines the misrouted cortical region calculated based on the overlap of right and left hemifields (Hoffmann et al., 2012, 2003). Panels B and C: two example probe maps ( $k$ -threshold = 100%) for voxels of the control (panel B) and an observer with albinism (panel C). The thresholded probe maps at 100%, 50%, 30% and 15% and the estimated  $pRF_{mp}$  are shown in Fig. S9. Fig. S10 shows that MP tends to perform better than the conventional bilateral pRF model for voxels with very low VE ( $<0.1$ ), which is in accordance with the results for healthy observers.

shows the histograms of the bilateral pRFs, which peak near the vertical meridians, conforming this observation.

#### 4. Discussion

In this study we introduced micro-probing (MP), a versatile, model-based fMRI analysis framework that requires only minimal *a priori* assumptions about the underlying biological mechanisms. By repetitively applying micro-probes to the fMRI time series, we produced a probe map that reveals the detailed visual field coverage of each voxel. These maps enable the extraction of fundamental pRF properties that were previously not accessible. We validated our approach using both empirical and simulated data and demonstrated its biological validity by revealing the highly atypical visual field representations for observers with albinism, without making any prior assumptions about this. Finally, we

demonstrated how various receptive field properties, such as shape and position, can be determined with relative ease for the entire visual cortex.

##### 4.1. MP is reliable, accurate and robust to noise

Our simulations and test-retest analysis were crucial to establish that MP-derived pRFs are reproducible and do not result from noise artefacts. Specifically, the test-retest analysis demonstrated that MP-derived probe maps are stable, reliable and highly consistent between the test and retest set. Moreover, the voxels whose agreement between the test and retest probe maps was low were associated with noisy signals.

The accuracy and robustness to noise was further assessed using a wide range of simulations. These showed: 1) MP could accurately detect multiple clusters and as well as their position and shape within a voxel; 2) MP was highly robust to noise and 3) the choice of clustering algorithm

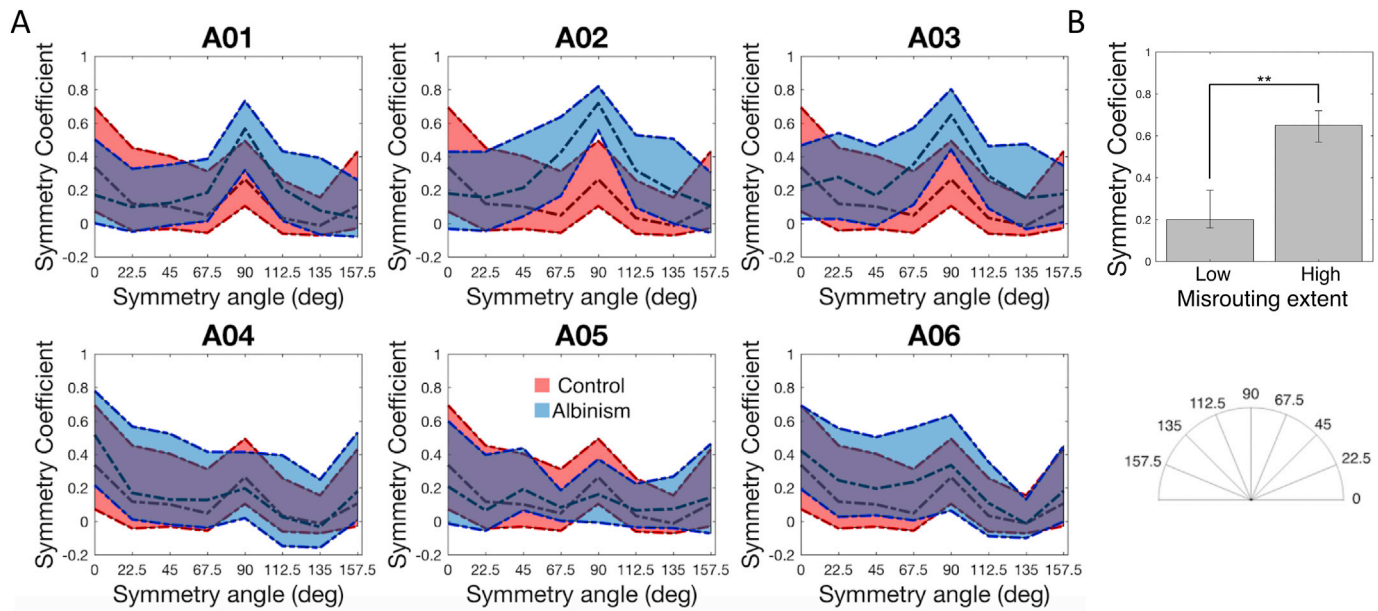


**Fig. 8. Symmetry coefficients based on probe maps.** Coefficients in healthy controls and albinism are shown as a function of the angle of the symmetry axis. Symmetry coefficients for the V1 of the right hemisphere during full field stimulation calculated across 8 symmetry axes (see right inset). The dashed lines represent the 5%, 50% and 95% confidence intervals. Albinism distributions are shown in blue and controls in red. Given that the inter- and intra-observer variability in healthy controls was low (see Fig. S11A), their symmetry coefficients were averaged. The albinism observers are shown in order of decreasing level of misrouting (see Table S2) as assessed independently (Ahmadi et al., 2019). Panel B: Bar graph representing the difference between the symmetry coefficient to the vertical meridian calculated for the observers with a low (A04, A05, A06) and a high (A01, A02, A03) coefficient. The misrouting extent classification of the observers with albinism was based on independent stimulation of the left and right hemisphere (Table S2).

had little to no effect on the number of clusters detected.

#### 4.2. MP recovers multiple subpopulations of RFs within a single voxel

Our analysis of empirical data of observers with albinism and simulations both revealed that MP accurately detects – for each voxel – the number of clusters as well as their position and shape. Applied to observers with albinism, MP resolved pRFs mirrored in the vertical meridian, thus revealing the simultaneous processing in one hemisphere of the signals coming from both the contralateral and ipsilateral hemifields. This corroborates previous studies that took the bilateral representation of the RFs as an *a priori* starting point (Hoffmann et al., 2012, 2003; Hoffmann and Dumoulin, 2015). Importantly, MP does not require making such an assumption. Instead, based on stimulation across the entire visual field, it quantifies the degree of symmetry in the vertical meridian (or other directions) in the probe maps.

As the next step, we used the symmetry values to quantify the extent of misrouting and identify the misrouted cortical region per observer. Remarkably, in controls, we showed that highly symmetric probe maps delineate the borders of the visual areas. The fact that MP revealed the atypical visual field representations in albinism suggests that the pRFs with multiple clusters found in controls are also biologically genuine and meaningful. MP therefore enables a straightforward estimation of atypical RF representations without requiring additional stimuli or assumptions.

In healthy observers, we demonstrated that MP not only resolves multiple clusters within a voxel, but also their properties. The clusters are spatially organized and the number of clusters increases with eccentricity. Note that due to cortical magnification, it is likely that the subpopulations are more widely spread in the periphery than in the fovea, and thus easier to identify. We found that approximately 10% of the estimated pRFs were bilateral and located near the vertical meridian. This supports the hypothesis that these bilateral pRF may derive from visual callosal connections that contribute to the integration of the cortical representation at the vertical midline (Choudhury et al., 1965;

Hubel and Wiesel, 1967; Makarov et al., 2008; Schmidt et al., 2010). Previous studies focusing on the medial superior temporal (MST) area also reported bilateral RFs (Raiguel et al., 1997; Saito et al., 1986; Ungerleider and Desimone, 1986). We also found multiple mirrored clusters (>2) in albinism, corroborating the finding in healthy observers (Fig. S12). This suggests two possible explanations that require further study: 1) that single neurons may simultaneously process information from distinct portions of the visual field and 2) subpopulations with spatially distinct properties may be present within a single voxel. Recent neuroimaging studies suggested that there are multiple subpopulations within a voxel that process different characteristics of the visual scene and consequently have different spatial properties. These findings together with current knowledge about the physiology of the visual cortex together support that the latter option is the most plausible (Le et al., 2017; Yildirim et al., 2018).

#### 4.3. MP is robust and recovers biologically meaningful RF properties with only minimal prior assumptions

The probe maps revealed that the pRFs can be heterogeneous in shape. MP enables pRF shape estimation without assuming specific shape properties *a priori*, such as circular symmetry. By assessing the statistical properties of the probe distributions, we showed how pRF shape can be characterized. Based on such assessments, we found that the majority of (Merkel et al., 2018; Silson et al., 2018b) the pRFs tend to be elongated. This is in line with recent studies that found that the pRFs tend to be elliptical and radially oriented towards the fovea (Merkel et al., 2018; Silson et al., 2018a). These findings support the functional differentiation of visual processing from fovea to periphery and across the ventral and dorsal cortical visual pathways.

By comparing the characteristics of MP derived pRFs to those of the conventional pRF, in healthy observers, the following three conclusions can be drawn. Firstly, the eccentricity estimates for pRFs<sub>mp</sub> and pRFs correlate closely. Our proposition that pRFs<sub>mp</sub> are biologically meaningful is supported by the similarity between the eccentricity maps

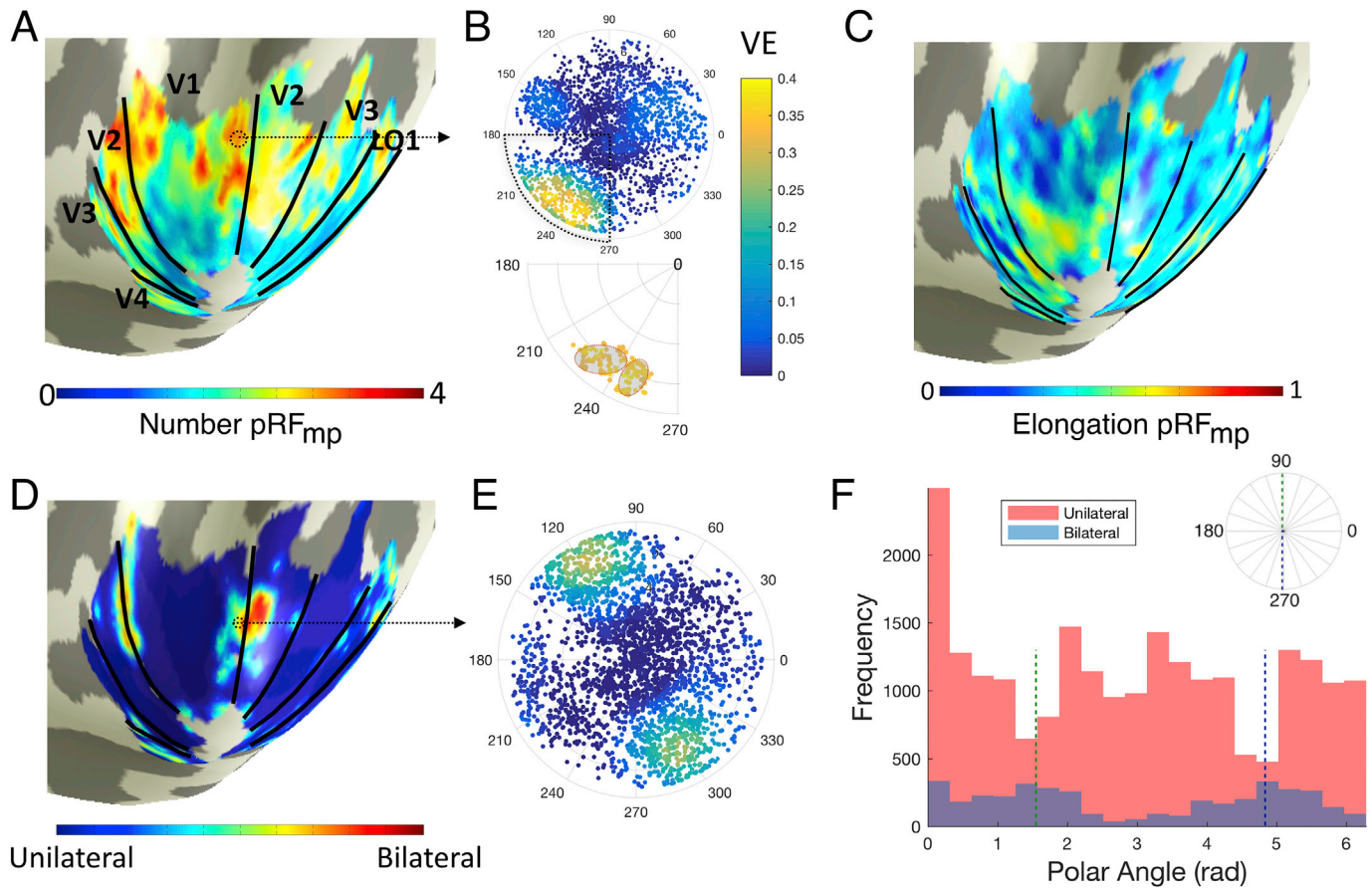


**Fig. 9.** Examples of  $pRF_{mp}$  properties estimated in the visual cortex of healthy observers. Panel A: Projection on an inflated brain mesh of the number of clusters estimated per voxel (right hemisphere of observer S07). Black lines represent the borders of visual areas. Panel B, upper part, shows an example of a MP map of a V1 voxel (location indicated by the dashed circle in Panel A); the lower part shows a zoomed-in view of one quarter field of the probe map indicating the estimated  $pRF_{mp}$  clusters (outlined by a red dashed line). Panel C: Projection on an inflated brain mesh of the  $pRF_{mp}$  elongation (right hemisphere of observer S07). Black lines indicate the borders of visual areas. Panel D: Projection on an inflated brain mesh of the unilateral-bilateral label, estimated per voxel. The intermediate colors between blue and red resulted from interpolation during mesh projection. Panel E: Probe map of a representative voxel with a bilateral RF (this was not mirrored in the vertical meridian, which differs from observers with albinism; location is indicated by the dashed circle in Panel D). Panel F: Histogram of the number of unilateral (red) and bilateral (blue)  $pRF$ s in V1 (14 hemispheres, 7 healthy observers). The dashed line depicts the vertical meridian.

obtained with the conventional  $pRF$  analysis and MP, and the fact that  $pRF_{mp}$  size increases with its eccentricity. In the periphery, however, estimated  $pRF_{mp}$  eccentricity tends to be smaller than conventional  $pRF$  eccentricity. This could be explained in part by the fact that  $pRF_{mp}$  size also tends to be smaller, which corroborates previous work showing that the smaller  $pRF$ s estimated for an orientation contrast stimulus also result in lower eccentricity estimates for the same voxels, especially in higher-order areas such as lateral occipital cortex (Yildirim et al., 2018). It may also reflect different model specifications. By design, the MP estimates are located within the stimulated visual field. Consequently, the  $pRF_{mp}$  estimates based on the probe maps are also situated within the stimulated part of the visual field. In contrast, the conventional  $pRF$  model allows for partially stimulated  $pRF$ s, the centers of which may be located far outside the stimulated visual field. Moreover, the differences between MP and conventional  $pRF$  mapping can also result from the model specifications. While in  $pRF$  mapping the optimal solution is found based on the parameters that result in the highest VE, MP is based on a VE weighted clustering. As a direct consequence, the  $pRF_{mp}$  definition depends on the number of probes taken into account ( $k$ -threshold) and on the scatter of these probes over the map.

Secondly, the level of specificity with which  $pRF_{mp}$ s are estimated is influenced by varying the  $k$ -threshold and VE-range for the probe maps. The results can range from retrieving many sub populations (very

restrictive  $k$ -threshold and VE-range) to more aggregate responses (more lenient  $k$ -threshold and VE-range). At the fairly restrictive  $k$ -threshold of 0.15 and VE-range of 0.1, the MP approach estimated smaller  $pRF_{mp}$ s than the conventional  $pRF$ . Such relatively small  $pRF_{mp}$ s are in agreement with other studies that also estimated significantly smaller  $pRF$  sizes than the conventional approach, for example using model-free approaches such as back projection (Greene et al., 2014; Keliris et al., 2019; Merkel et al., 2018) or second order stimuli (Yildirim et al., 2018). Thirdly, compared to conventional methods, MP improves the capture of the dynamics of the measured signal, especially for voxels with signals that have a relatively low explanatory power. We also determined that the  $pRF_{mp}$  estimations are robust to noise, as MP could be performed reliably despite the presence of nystagmus in the observers with albinism.

When is MP a good procedure to use? For simply delineating visual areas, MP does not represent a significant advantage compared to the conventional  $pRF$  method. Yet, we promote the use of MP when “you can expect the unexpected”, i.e. when study outcomes are unpredictable or may rely on aggregate RFs characteristics. In particular, this would apply to studies on: 1) neurodevelopment and neuroplasticity, 2) ophthalmic and neurological pathologies, and 3) cognitive effects. Moreover, MP can be useful for visualization of the data underlying any  $pRF$  estimates and meticulous data cleaning.



#### 4.4. Limitations

We identified multiple clusters in voxels in healthy observers, but the functional implications of this finding are uncertain. We have assumed that clusters have biological relevance, but some of the units may have resulted from artefacts related to segmentation, from voxels stranded on the cortical sulci, or from partial voluming. There are several ways in which the effect of such artefacts could be reduced: correcting for partial voluming (Dukart and Bertolino, 2014), identifying and extracting local sulci (Fracasso et al., 2016; Zhou et al., 1999) and applying MP to higher resolution functional data ( $<1$  mm isotropic). Using more precisely controlled stimuli will contribute to unravelling the biological significance of the multiple clusters and characterizing the neuronal subpopulations specialized in the processing of specific spatial and temporal properties (orientation, spatial frequency, colour etc) (Klein et al., 2014; Le et al., 2017; Yildirim et al., 2018).

At present, MP is a computationally intensive approach when compared to the conventional pRF model. We expect that software optimization and advances in hardware will contribute to reducing the computation time. We currently address this issue by using parallel GPU computing. Furthermore, the use of MCMC sampling is needed only to speed up the process/limiting computing resource use, but is not fundamental to MP. In principle, probe maps could result from systematically probing every position in stimulus space, creating a densely covered probe map for each voxel. The use of a Markov-Chain means that the current probe maps contain more probes for regions with higher VE. Our current estimate of pRF<sub>mp</sub> shape is based on the clustering of the probes weighted by their VE. In contrast, pRFs are fitted to explain the VE of the signal. This explains why the pRFs<sub>mp</sub> shapes sometimes differ (e.g. they are more elongated) from the pRFs. In our view, neither is necessarily correct; they are just different ways to assess shape. Future work will be required to indicate which approach best approximates biological reality.

#### 4.5. Future directions

MP as presented here is a reliable and versatile method to study cortical organization, but it can still be improved in several ways. First, using more efficient stimulus designs, such as a narrower bar or multi-focal stimulation (Binda et al., 2013; Senden et al., 2014), could improve the performance of MP. Secondly, applying additional advanced data-driven metrics to extract the shape and number of clusters may result in a more detailed characterization of the RF. Thirdly, the definition of a probe could be extended, for example to a difference of Gaussians, which may enable MP to also account for negative blood oxygen level dependent (BOLD) activity (Zuiderbaan et al., 2012).

Previous studies have shown that pRF properties are not stable, and may change in response to environmental factors (stimulus, task) and cognitive factors such as attention (Klein et al., 2014; Le et al., 2017; Yildirim et al., 2018). Given that the probe maps reflect the scatter in the location of the receptive field centers, this scatter may reveal the dynamic properties of the pRFs (changes in position) and could be related to the connections underlying the RFs. Moreover, in principle, MP could be extended to cortico-cortical models, such as connective field modelling (Haak et al., 2013), which would also enable fine-grained mapping of the flow of information between brain areas.

Changes in pRFs have been reported in health and disease (for a summary see (Dumoulin and Knapen, 2018)). Regarding disease, this concerns differentiation following cortical and retinal lesions, schizophrenia and autism spectrum disorder. We anticipate that the application of MP to ophthalmologic and neurologic disorders as well as to adaptation studies will reveal additional characteristics of the RF structure, such as number and shape.

The recent development of ultra-high field fMRI enables the in-vivo examination of the human brain at a mesoscale and can reveal previously unmapped columnar organizations. However, there is a need for

methods that can extract more detailed information on the structure and function of the cortex from this high-resolution data. The application of MP to high-resolution functional data has the potential to reveal how the clusters and their properties are distributed across cortical depth. This will be crucial to study the functional differentiation of the visual processing across laminae. Moreover, it may complement previous studies of cortical organization across cortical depth, ocular dominance and columnar pinwheel organization for orientation selectivity (Fracasso et al., 2018; Shmuel et al., 2007; Yacoub et al., 2008).

In this study, we described the application of MP to characterize the spatial organization of the visual cortex. However, MP could also be applied to visual feature dimensions, other sensory modalities and non-spatial yet spatially organized features such as numerosity (Harvey et al., 2015; Thomas et al., 2015).

#### 5. Conclusion

MP is a versatile, model-based fMRI analysis framework that can reveal multiple, biologically meaningful subpopulations of RFs within a single voxel. Consequently, it enables a highly detailed characterization of RF properties (symmetry, skewness and elongation), which was previously unattainable. The existence of multiple pRF<sub>mp</sub> clusters indicates that voxels capture the activity of multiple subpopulations of neurons that may sample from different regions of the visual field. MP thus enables a detailed characterization of the temporal, spatial and functional properties of the brain in health and disease using minimal *a priori* assumptions.

#### Declaration of competing interest

None.

#### Acknowledgments

We thank Koen V. Haak for suggesting to apply MP to albinism data. Authors JC, KA and AI were supported by the European Union's Horizon 2020 research and innovation programme under the Marie Skłodowska-Curie grant agreements No. 641805 (NextGenVis) and No. 661883 (EGRET) awarded to FWC and MBH. The funding organization had no role in the design, conduct, analysis, or publication of this research.

#### Appendix A. Supplementary data

Supplementary data to this article can be found online at <https://doi.org/10.1016/j.neuroimage.2019.116423>.

#### References

- Adaszewski, S., Slater, D., Melie-Garcia, L., Draganski, B., Bogorodzki, P., 2018. Simultaneous estimation of population receptive field and hemodynamic parameters from single point BOLD responses using Metropolis-Hastings sampling. *Neuroimage* 172, 175–193.
- Ahmadi, K., Herbig, A., Wagner, M., Kanowski, M., Thieme, H., Hoffmann, M.B., 2019. Population receptive field and connectivity properties of the early visual cortex in human albinism. *Neuroimage* 202, 105–116.
- Azzopardi, P., Cowey, A., 1993. Preferential representation of the fovea in the primary visual cortex. *Nature* 361, 719–721.
- Baseler, H.A., Gouws, A., Haak, K.V., Racey, C., Crossland, M.D., Tufail, A., Rubin, G.S., Cornelissen, F.W., Morland, A.B., 2011. Large-scale remapping of visual cortex is absent in adult humans with macular degeneration. *Nat. Neurosci.* 14, 649–655.
- Binda, P., Thomas, J.M., Boynton, G.M., Fine, I., 2013. Minimizing biases in estimating the reorganization of human visual areas with BOLD retinotopic mapping. *J. Vis.* 13, 13.
- Boynton, G.M., Demb, J.B., Heeger, D.J., 1996. fMRI responses in human V1 correlate with perceived stimulus contrast. *Neuroimage* 3, S265.
- Brainard, D., 1997. The Psychophysics Toolbox. *Spat. Vis.* 10, 433–436.
- Chapin, J.K., 1986. Laminar differences in sizes, shapes, and response profiles of cutaneous receptive fields in the rat SI cortex. *Exp. Brain Res.* 62, 549–559.
- Choudhury, B.P., Whitteridge, D., Wilson, M.E., 1965. The function of callosal connections of the visual cortex. *Q. J. Exp. Physiol. Cogn. Med. Sci.* 50, 214–219.

- Dale M., A., Fischl, B., Sereno I., M., 1999. Cortical surface-based analysis. I. Segmentation and surface reconstruction. *Neuroimage* 9, 179–194.
- Davies, D.L., Bouldin, D.W., 1979. A cluster separation measure. *IEEE Trans. Pattern Anal. Mach. Intell.* 1, 224–227.
- DeValois, R.L., 1982. Early visual processing: feature detection or spatial filtering?. In: *Lecture Notes in Biomathematics*, pp. 152–174.
- Dukart, J., Bertolino, A., 2014. When structure affects function – the need for partial volume effect correction in functional and resting state magnetic resonance imaging studies. *PLoS One*. <https://doi.org/10.1371/journal.pone.0114227>.
- Dumoulin, S.O., Knapen, T., 2018. How visual cortical organization is altered by ophthalmologic and neurologic disorders. *Annu Rev Vis Sci* 4, 357–379.
- Dumoulin, S.O., Wandell, B.A., 2008. Population receptive field estimates in human visual cortex. *Neuroimage* 39, 647–660.
- Finlay, B.L., Schiller, P.H., Volman, S.F., 1976. Meridional differences in orientation sensitivity in monkey striate cortex. *Brain Res.* 105, 350–352.
- Fracasso, A., Luijten, P.R., Dumoulin, S.O., Petridou, N., 2018. Laminar imaging of positive and negative BOLD in human visual cortex at 7 T. *Neuroimage* 164, 100–111.
- Fracasso, A., van Veluw, S.J., Visser, F., Luijten, P.R., Spliet, W., Zwanenburg, J.J.M., Dumoulin, S.O., Petridou, N., 2016. Lines of Baillarger in vivo and ex vivo: myelin contrast across lamina at 7 T MRI and histology. *Neuroimage*. <https://doi.org/10.1016/j.neuroimage.2016.02.072>.
- Friston, K.J., 1998. Modes or models: a critique on independent component analysis for fMRI. *Trends Cogn. Sci.* 2, 373–375.
- Greene, C.A., Dumoulin, S.O., Harvey, B.M., Ress, D., 2014. Measurement of population receptive fields in human early visual cortex using back-projection tomography. *J. Vis.* 14 <https://doi.org/10.1167/14.1.17>.
- Haak, K.V., Cornelissen, F.W., Morland, A.B., 2012. Population receptive field dynamics in human visual cortex. *PLoS One* 7, e37686.
- Haak, K.V., Winawer, J., Harvey, B.M., Renken, R., Dumoulin, S.O., Wandell, B.A., Cornelissen, F.W., 2013. Connective field modeling. *Neuroimage* 66, 376–384.
- Harvey, B.M., Fracasso, A., Petridou, N., Dumoulin, S.O., 2015. Topographic representations of object size and relationships with numerosity reveal generalized quantity processing in human parietal cortex. *Proc. Natl. Acad. Sci. U. S. A.* 112, 13525–13530.
- Hoffmann, M.B., Dumoulin, S.O., 2015. Congenital visual pathway abnormalities: a window onto cortical stability and plasticity. *Trends Neurosci.* 38, 55–65.
- Hoffmann, M.B., Kaule, F.R., Levin, N., Masuda, Y., Kumar, A., Gottlob, I., Horiguchi, H., Dougherty, R.F., Stadler, J., Wolynski, B., Speck, O., Kanowski, M., Liao, Y.J., Wandell, B.A., Dumoulin, S.O., 2012. Plasticity and stability of the visual system in human achiasma. *Neuron* 75, 393–401.
- Hoffmann, M.B., Tolhurst, D.J., Moore, A.T., Morland, A.B., 2003. Organization of the visual cortex in human albinism. *J. Neurosci.* 23, 8921–8930.
- Hubel, D.H., Wiesel, T.N., 1974a. Uniformity of monkey striate cortex: a parallel relationship between field size, scatter, and magnification factor. *J. Comp. Neurol.* 158, 295–305.
- Hubel, D.H., Wiesel, T.N., 1974b. Sequence regularity and geometry of orientation columns in the monkey striate cortex. *J. Comp. Neurol.* 158, 267–293.
- Hubel, D.H., Wiesel, T.N., 1967. Cortical and callosal connections concerned with the vertical meridian of visual fields in the cat. *J. Neurophysiol.* 30, 1561–1573.
- Hubel, D.H., Wiesel, T.N., Stryker, M.P., 1977. Orientation columns in macaque monkey visual cortex demonstrated by the 2-deoxyglucose autoradiographic technique. *Nature* 269, 328–330.
- Kaule, F.R., Wolynski, B., Gottlob, I., Stadler, J., Speck, O., Kanowski, M., Meltendorf, S., Behrens-Baumann, W., Hoffmann, M.B., 2014. Impact of chiasma opticum malformations on the organization of the human ventral visual cortex. *Hum. Brain Mapp.* 35, 5093–5105.
- Keliris, G.A., Li, Q., Papanikolaou, A., Logothetis, N.K., Smirnakis, S.M., 2019. Estimating average single-neuron visual receptive field sizes by fMRI. *Proc. Natl. Acad. Sci. U. S. A.* 116, 6425–6434.
- Klein, B.P., Harvey, B.M., Dumoulin, S.O., 2014. Attraction of position preference by spatial attention throughout human visual cortex. *Neuron* 84, 227–237.
- Le, R., Witthoft, N., Ben-Shachar, M., Wandell, B., 2017. The field of view available to the ventral occipito-temporal reading circuitry. *J. Vis.* 17, 6.
- Makarov, V.A., Schmidt, K.E., Castellanos, N.P., Lopez-Aguado, L., Innocenti, G.M., 2008. Stimulus-dependent interaction between the visual areas 17 and 18 of the 2 hemispheres of the ferret (*Mustela putorius*). *Cerebr. Cortex* 18, 1951–1960.
- Merkel, C., Hopf, J.-M., Schoenfeld, M.A., 2018. Spatial elongation of population receptive field profiles revealed by model-free fMRI back-projection. *Hum. Brain Mapp.* 39, 2472–2481.
- Nestares, O., Heeger, D.J., 2000. Robust multiresolution alignment of MRI brain volumes. *Magn. Reson. Med.* 43, 705–715.
- Papanikolaou, A., Keliris, G.A., Papageorgiou, T.D., Shao, Y., Krapp, E., Papageorgiou, E., Stingl, K., Bruckmann, A., Schiefer, U., Logothetis, N.K., Smirnakis, S.M., 2014. Population receptive field analysis of the primary visual cortex complements perimetry in patients with homonymous visual field defects. *Proc. Natl. Acad. Sci. U. S. A.* 111, E1656–E1665.
- Pelli G., D., 1997. The VideoToolbox software for visual psychophysics: transforming numbers into movies. *Spat. Vis.* 10, 437–442.
- Raiguel, S., Van Hulle, M.M., Xiao, D.K., Marcar, V.L., Lagae, L., Orban, G.A., 1997. Size and shape of receptive fields in the medial superior temporal area (MST) of the macaque. *Neuroreport* 8, 2803–2808.
- Ringach, D.L., 2002. Spatial structure and symmetry of simple-cell receptive fields in macaque primary visual cortex. *J. Neurophysiol.* 88, 455–463.
- Saito, H., Yukie, M., Tanaka, K., Hikosaka, K., Fukada, Y., Iwai, E., 1986. Integration of direction signals of image motion in the superior temporal sulcus of the macaque monkey. *J. Neurosci.* 6, 145–157.
- Schmidt, K.E., Lomber, S.G., Innocenti, G.M., 2010. Specificity of neuronal responses in primary visual cortex is modulated by interhemispheric corticocortical input. *Cerebr. Cortex* 20, 2776–2786.
- Senden, M., Reithler, J., Gijzen, S., Goebel, R., 2014. Evaluating population receptive field estimation frameworks in terms of robustness and reproducibility. *PLoS One* 9, e114054.
- Shmuel, A., Yacoub, E., Chaimow, D., Logothetis, N.K., Ugurbil, K., 2007. Spatio-temporal point-spread function of fMRI signal in human gray matter at 7 Tesla. *Neuroimage* 35, 539–552.
- Silson, E.H., Reynolds, R.C., Kravitz, D.J., Baker, C.I., 2018a. Differential sampling of visual space in ventral and dorsal early visual cortex. *J. Neurosci.* 38, 2294–2303.
- Silson, E.H., Reynolds, R.C., Kravitz, D.J., Baker, C.I., 2018b. Differential sampling of visual space in ventral and dorsal early visual cortex. *J. Neurosci.* 38, 2294–2303.
- Thomas, J.M., Huber, E., Stecker, G.C., Boynton, G.M., Saenz, M., Fine, I., 2015. Population receptive field estimates of human auditory cortex. *Neuroimage* 105, 428–439.
- Tibshirani, R., Walther, G., Hastie, T., 2001. Estimating the number of clusters in a data set via the gap statistic. *Journal of the Royal Statistical Society: Series B (Statistical Methodology)* 63, 411–423.
- Ungerleider, L.G., Desimone, R., 1986. Projections to the superior temporal sulcus from the central and peripheral field representations of V1 and V2. *J. Comp. Neurol.* 248, 147–163.
- Wandell, B.A., Chial, S., Backus, B.T., 2000. Visualization and measurement of the cortical surface. *J. Cogn. Neurosci.* 12, 739–752.
- Wandell, B.A., Smirnakis, S.M., 2009. Plasticity and stability of visual field maps in adult primary visual cortex. *Nat. Rev. Neurosci.* 10, 873–884.
- Yacoub, E., Harel, N., Ugurbil, K., 2008. High-field fMRI unveils orientation columns in humans. *Proc. Natl. Acad. Sci. U. S. A.* 105, 10607–10612.
- Yildirim, F., Carvalho, J., Cornelissen, F.W., 2018. A second-order orientation-contrast stimulus for population-receptive-field-based retinotopic mapping. *Neuroimage* 164, 183–193.
- Zeidman, P., Silson, E.H., Schwarzkopf, D.S., Baker, C.I., Penny, W., 2018. Bayesian population receptive field modelling. *Neuroimage* 180, 173–187.
- Zhou, Y., Thompson, P.M., Toga, A.W., 1999. Extracting and representing the cortical sulci. *IEEE Comput. Graph. Appl.* 19, 49–55.
- Zuiderbaan, W., Harvey, B.M., Dumoulin, S.O., 2012. Modeling center-surround configurations in population receptive fields using fMRI. *J. Vis.* 12, 10.